A&A 483, 769–781 (2008)
DOI: 10.1051/0004-6361:20078899

Astronomy & Astrophysics

Evidence for metallicity spreads in three massive M 31 globular clusters⋆,⋆⋆

I. Fuentes-Carrera[1,2], P. Jablonka[1,3,4], A. Sarajedini[5], T. Bridges[6], G. Djorgovski[7], and G. Meylan[4]

[1] GEPI, Observatoire de Paris, CNRS, Université Paris Diderot, 5 place Jules Janssen, 92190, Meudon, France
e-mail: isaura.fuentes@obspm.fr
[2] Instituto de Astronomía, Geofísica e Ciencias Atmosféricas, Universidade de São Paulo, Rua do Matão 1226-Cidade Universitária, 05508-900 São Paulo SP, Brazil
[3] Observatoire, Université de Genève, chemin des Maillettes 51, 1290 Sauverny, Switzerland
e-mail: Pascale.Jablonka@obs.unige.ch
[4] Laboratoire d'Astrophysique, Ecole Polytechnique Fédérale de Lausanne (EPFL), Observatoire, 1290 Sauverny, Switzerland
e-mail: georges.meylan@epfl.ch
[5] University of Florida, Department of Astronomy, Gainesville, FL 32611, USA
e-mail: ata@astro.ufl.edu
[6] Department of Physics, Engineering Physics, and Astronomy, Queen's University, Kingston, ON K7L 3N6, Canada
e-mail: tjb@astro.queensu.ca
[7] California Institute of Technology, Pasadena, CA 91125, USA
e-mail: george@astro.caltech.edu

Received 22 October 2007 / Accepted 14 March 2008

ABSTRACT

Aims. We quantify the intrinsic width of the red giant branches of three massive globular clusters in M 31 in a search for metallicity spreads within these objects.
Methods. We present HST/ACS observations of three massive clusters in M 31, G78, G213, and G280. A thorough description of the photometry extraction and calibration is presented. After derivation of the color−magnitude diagrams, we quantify the intrinsic width of the red giant branch of each cluster.
Results. This width translates into a metallicity dispersion that indicates a complex star formation history for this type of system. For G78, $\sigma_{[Fe/H]} = 0.86 \pm 0.37$; for G213, 0.89 ± 0.20; and for G280, 1.03 ± 0.26. We find that the metallicity dispersion of the clusters does not scale with mean metallicity. We also find no trend with the cluster mass. We discuss some possible formation scenarios that would explain our results.

Key words. galaxies: evolution – galaxies: Local Group – galaxies: star clusters – Galaxy: globular clusters: general

1. Introduction

There are now a few dozen Galactic globular clusters for which high resolution spectroscopy has allowed insight into their star-to-star chemical variations (Gratton et al. 2004). Omega Centauri (ω Cen) appears to be the only case where such variations are clear for all elements. Several scenarios have been proposed to explain these observations: The high primordial mass of ω Cen might be enough to induce secondary star formation (Dopita & Smith 1986). Models of chemical evolution have considered self enrichment scenarios (Ikuta & Arimoto 2000; Tsujimoto & Shigeyama 2003). Primordial chemical inhomogeneities have also been investigated (e.g., Kraft 1994). Finally, the possibility that ω Cen is the nucleus of a now-dissolved nucleated dwarf galaxy has been raised by a number of studies (Zinnecker et al. 1988; Lee et al. 1999; Hilker & Richtler 2000).

Our knowledge of extragalactic globular clusters is currently far less advanced. At the moment, the globular cluster G1 in the halo of M 31 constitutes the only evidence for a metallicity spread, as derived from the width of its red giant branch (RGB) (Meylan et al. 2001). The parallel with ω Cen is immediate. Both clusters exhibit a metal abundance range of about 1 dex, G1 being twice as massive as ω Cen. The two clusters differ in a number of ways though, which are likely important clues to the understanding of their formation. For example, G1 and ω Cen have very different locations with respect to their host galaxy – G1 is a halo cluster located in projection at ∼40 kpc from the center of M 31 (nearly the distance between our Galaxy and the LMC), while ω Cen is now at ∼6 kpc from the Galactic center and at ∼1 kpc from the Galactic plane.

Although ω Centauri is by far the brightest and most massive globular cluster in our Galaxy, G1 may not be the only such massive cluster belonging to M 31. There are at least three other bright clusters which have central velocity dispersions larger than 20 km s^{-1} (Djorgovski et al. 1997). They offer a unique opportunity to investigate the degree to which the mass of a globular cluster influences its chemical evolution. In the velocity dispersion *versus* absolute magnitude relation (the equivalent for globular clusters of the Faber-Jackson relation), the two

⋆ Tables of individual photometric measurements are available at the CDS via anonymous ftp to
cdsarc.u-strasbg.fr (130.79.128.5) or via
http://cdsweb.u-strasbg.fr/cgi-bin/qcat?J/A+A/483/769
⋆⋆ Figures 4 and 5 are only available in electronic form at
http://www.aanda.org

Table 1. Properties of observed clusters.

Cluster	α (2000) (1)	δ (2000) (2)	V(mag) (3)	$D_{M31}(')$ (4)	[Fe/H] (5)	σ(km s^{-1}) (6)	$E(B-V)$ (7)
G78	00 41 01.2	+41 13 45.5	14.2	19.2	−0.92	25.48	0.23
G213	00 43 14.4	+41 07 20.5	14.5	11.2	−1.08	20.50	0.10
G280	00 44 29.5	+41 21 35.8	14.3	20.5	−0.70	25.94	0.10

References: (3) and (5) Huchra et al. (1991); (6) Djorgovski et al. (1997); (7) Jablonka et al. (1992), for G78, this work for G213, Frogel et al. (1980), for G280.

sequences of Galactic and M 31 systems show no detectable difference in the slope and zero-point of their correlations. Thanks to the similarity between the Galactic and M 31 globular cluster sequences, any conclusion drawn from additional M 31 clusters may represent general (universal) characteristics.

We present here the analysis of images obtained with the Advanced Camera for Surveys aboard the Hubble Space Telescope of those three massive and bright clusters in M 31. Our goal is to quantify the intrinsic width of their red giant branches in order to search for any metallicity spread.

2. Observations and data reduction

2.1. Sample selection

Velocity dispersions are a good indicator of dynamical mass for old stellar systems with nearly constant mass-to-light (M/L) ratios, such as globular clusters (Djorgovski & Meylan 1994; Djorgovski et al. 1997). Therefore, our selection criterion for this work operates via the cluster total luminosities and velocity dispersions.

As mentioned previously, apart from G1, three other clusters among the 21 objects in the sample of Djorgovski et al. (1997) have central velocity dispersions, σ, greater than 20 km s^{-1}. Figure 1 shows the location of the three clusters in M 31. All three of them are located off the major axis of M 31 towards the minor axis. G78 is located (in projection) on the edge of a dust cloud (object D48 in Hodge 1981) which lies northwest of the cluster. G213 coincides in projection with one of M 31's spiral arms but does not lie near any particular dust cloud or stellar association. G280 is also located at the edge of a dust cloud (object D642) lying to the northeast of the cluster. Table 1 lists some of the properties of these clusters. Columns (1) and (2) give the coordinates of each cluster, Col. (3) the magnitude in the V filter (Huchra et al. 1991), Col. (4) the projected distance from the center of M 31, Col. (5) the metallicity (Huchra et al. 1991), Col. (6) the velocity dispersion (Djorgovski et al. 1997) and Col. (7) the reddening value (Jablonka et al. 1992, for G78; this work for G213; Frogel et al. 1980, for G280).

2.2. Observations

Observations of the three clusters and their surrounding fields were obtained with the High Resolution Channel (HRC) of the Advanced Camera for Surveys (ACS) aboard HST (Cycle 12; program ID 9719). The HRC has a plate scale of 0.027″ pixel^{-1} and a field of view (FoV) of 26″ × 29″. Four images of each globular cluster were taken using the *F606W* (close to *V*) and *F814W* (close to *I*) filters with total integration time of 505 × 4 = 2020 s and 715 × 4 = 2860 s, respectively. In order to be able to detect cosmic rays and other artifacts as well as to sample the PSF optimally, images were dithered following the four-point dither pattern known as ACS-HRC-DITHER-BOX with a step of 0.15″ each[1].

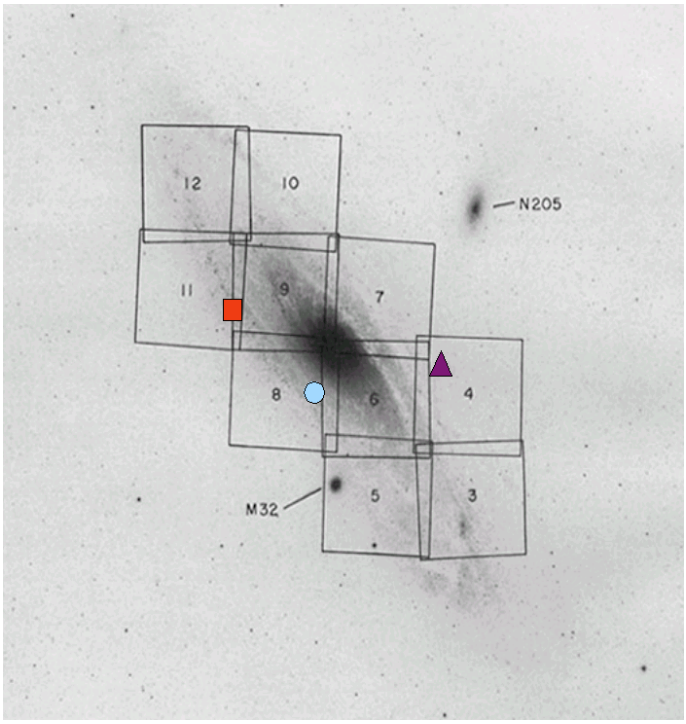

Fig. 1. Location of globular clusters in M 31. Dark purple triangle corresponds to the location of G78, light blue circle corresponds to G213 and dark red square shows the location of G280. Numbered squared regions correspond to charts in the Atlas of the Andromeda Galaxy (Hodge 1981).

For each cluster, we used the FLT images downloaded from the HST archive. The instrumental signature has been removed from these images (bias, dark and flat-field correction) by the on-the-fly-reprocessing (*OTFR*) performed by *CALACS*. These FLT images were then corrected for geometric distortion and combined using the *MultiDrizzle* task of the STSci pipeline incorporated in PyRAF (Koekemoer et al. 2002). This procedure eliminated all of the cosmic rays and bad pixels on the images. We have used the default values for all of the parameters in the *MultiDrizzle* task. We used "median" as the IMCOMBINE method in order to add up the four images per filter. Due to a gradient in the background of the ACS field, images were not sky-subtracted. Background variation was dealt with during the photometry extraction using DAOPHOT (Sect. 3). No oversampling was done when drizzling the images into the final image to avoid introducing a second redistribution of noise in the resampled pixels. Figure 2 shows the final *MultiDrizzled* image of

[1] See the ACS Phase II Proposal Instructions http://www.stsci.edu/hst/acs/proposing/dither for further details

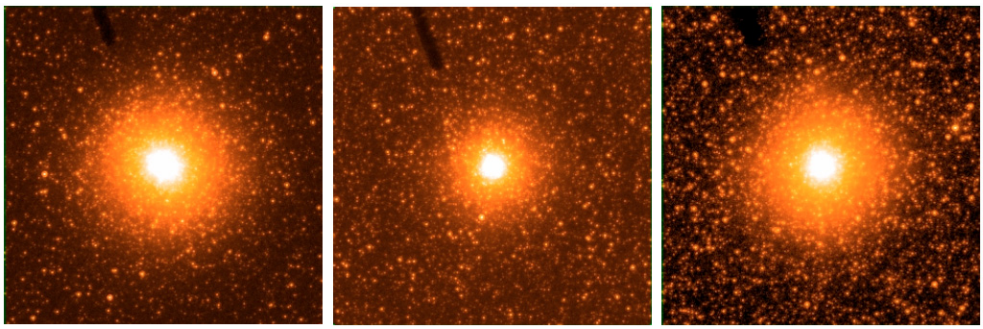

Fig. 2. *MultiDrizzled* images of G78 (*left*), G213 (*middle*) and G280 (*right*) and surrounding field stars in the *F814W* filter. North is to the top, East is to the left. The dark feature seen on the northeast corresponds to the occulting finger of the ACS. Field of view (FoV) for each cluster is $17.3'' \times 17.3''$.

each cluster in the *F814W* filter. The long, dark feature on each image is the shadow of the occulting finger of the ACS/HRC coronagraph. A quick comparison of these images shows that G78 is bigger than G213 and G280 which are rather similar in size and structure. All of them have a dense core, though proportionally, the core of G78 is smaller with respect to the cluster as a whole. The field surrounding G213 is the most populated. Both of the fields surrounding G78 and G280 are sparse, although that of G78 seems to be somewhat less populated.

3. Photometry

3.1. Photometry Extraction

Photometry was determined using the DAOPHOT/ALLSTAR routines (Stetson 1994). Since *MultiDrizzled* images are produced in units of electrons s^{-1} $pixel^{-1}$, they need to be multiplied by the exposure time and divided by the gain factor to get back to the original ADU $pixel^{-1}$ units used by DAOPHOT and ALLSTAR. In order to do so we need to consider how many original images are included in the drizzled images. If N images have been combined by the drizzle routine, then the read noise is reduced by a factor between 1 and $\sqrt{N}$, and the gain is increased by a factor between 1 and N. Unfortunately these numbers are not necessarily constant because any one pixel in the drizzled image can come from as few as 1 or as many as N original images. One must also consider the fact that the *MultiDrizzle* task redistributes the noise in each pixel of the image, while DAOPHOT assumes that the noise properties of an image are approximately constant everywhere. In order to take these effects into account in the derivation of precision photometry, we followed P. Stetson's suggestion and modified our initial values for the READ OUT NOISE and the GAIN in both the DAOPHOT and ALLSTAR routines in order to have χ^2 values close to 1. Object detection was done with DAOFIND on the combined *MultiDrizzled* image. Point-spread functions (PSFs) were constructed with DAOPHOT and stars were measured using the ALLSTAR routine. The PSF of each cluster on each filter was built from bright isolated stars in the FoV. For G213 and G280, the PSF for the *F606W* image was best determined using a few, bright and isolated stars (23 for G213 and 25 stars for G280) while for the *F814W* image, the PSF was better computed using more stars (52 for G213 and 47 stars for G280). For G78, both PSFs were best determined using a small number of stars (22 stars for both images). For the three clusters, the stars used to estimate the PSF cover the whole FoV except for the central parts of the FoV (about 2 arcsec from the center of the FoV). As a first approach, we used a PSF that varied linearly across the FoV in case there still remained a slight variation of the pixel scales due to the optics of the ACS. Through the analysis of residuals after star subtraction, we found that the photometry was best achieved using a spatially constant PSF, which supports the fact that the pixel variation was properly corrected by the *MultiDrizzle* procedure.

The individual photometric measurements for each FoV are available at the CDS, Table 2 shows a sample of the data. Column (1) indicates the ID number given by DAOPHOT, Cols. (2) and (3) indicate the star coordinates (in pixels) in the *F814W* filter image, Cols. (4) to (7) give the instrumental magnitude in the *F606W* filter, its associated error, χ^2 and sharpness, respectively, while Cols. (8) to (11) display the instrumental magnitude in the *F814W* filter, its associated error, χ^2 and sharpness, respectively. Column (12) indicates if the star survived the statistical selection discussed in Sect. 4. A value of 1 indicates the star survived the selection, a value of zero indicates the star was rejected for the rest of the analysis.

3.2. Photometric calibration

Once the instrumental photometry was extracted, it was necessary to convert it to the STMAG system (Koornef et al. 1986). In order to do so, the *MultiDrizzled* nature of the images must be taken into account. Our *MultiDrizzled* images were obtained by *drizzling* N FLT images into a single image. FLT images have units of electrons while the *MultiDrizzled* image is in units of electrons s^{-1}. Photometry was extracted using the DAOPHOT and ALLSTAR packages which work with ADU. As previously mentioned, in order to work with a *MultiDrizzled* image using these packages, we multiplied the original *MultiDrizzled* image by the exposure time of one FLT image, t_{exp}, and divided it by the gain of the CCD, $gain_{ccd}$[2]. We shall call the resulting image, the *modified Multidrizzled* image.

3.2.1. Charge efficiency transfer corrections

Photometric losses due to the problem of charge transfer efficiency (CTE) of the CCD need to be quantified before converting instrumental magnitudes to any photometric standard system. For the ACS/HRC, the CTE correction is given by the formula in the ACS Data Handbook[3]. In order to have the correct input values, the SKY brightness obtained with ALLSTAR from the *modified MultiDrizzled* image in ADU, must be multiplied

[2] This can only be done if ALL FLT images used in the *drizzling* process have the same exposure time, t_{exp}.

[3] Chapter 6, Sect. 1.5.

Table 2. Individual photometric measurements for a sample of stars in the FoV of G78. All photometric measurements for the FoVs of the three clusters are available in electronic form at the CDS.

ID	*X* (px)	*Y* (px)	*F606W* mag	*F606W* error	*F606W* chi^2	*F606W* sharpness	*F814W* mag	*F814W* error	*F814W* chi chi^2	*F814W* sharpness	selection FLAG
(1)	(2)	(3)	(4)	(5)	(6)	(7)	(8)	(9)	(10)	(11)	(12)
500.	534.66	87.15	19.3920	0.05770	0.92800	0.16100	19.0470	0.05580	1.12000	0.14300	0
505.	287.55	87.88	19.4300	0.05890	0.92100	0.04500	20.0100	0.08720	0.75200	–0.11500	1
533.	280.98	90.67	18.6160	0.02680	0.71900	0.06200	18.4820	0.03030	0.88300	0.11800	0
1410.	286.32	185.18	19.8010	0.04260	0.43300	0.02900	20.1830	0.08080	0.60800	–0.08700	1
1418.	638.02	185.86	19.1530	0.04340	0.81300	0.09000	18.9620	0.03350	0.64600	0.17600	0
1434.	800.98	187.72	19.3000	0.05000	0.83900	0.10700	18.9020	0.03700	0.76400	0.17400	1
1449.	797.39	189.19	20.7160	0.15410	0.83300	0.59500	20.5640	0.10430	0.53400	–0.15900	1

by the gain of the CCD. On the other hand, the FLUX of the star (in electrons) is the original flux on the FLT image. This flux is equal to the flux associated to the magnitude given by DAOPHOT, MAG_{modDRZ}(star), times the gain of the CCD, $gain_{ccd}$. Considering that DAOPHOT adds a zeropoint of 25.0 to all magnitudes, the resulting flux is given by

$$\text{FLUX (electrons)} = 10^{-(MAG_{modDRZ}(star)-25.0)/2.5} \times gain_{ccd}. \quad (1)$$

Once the SKY and FLUX values have been corrected, the resulting CTE correction (YCTE) will be that for a single FLT image.

3.2.2. Aperture corrections

Our aim is to transform the magnitudes obtained from ALLSTAR, which we will call *PSF magnitudes*, into magnitudes in the STMAG system. In order to do so, several aperture corrections need to be made. Before being converted into magnitudes in an aperture with "infinite" radius, *PSF magnitudes* need to be corrected to magnitudes in an aperture of radius 0.5″ (18.5 HRC pixels). Since the aperture corrections used to transform instrumental magnitudes into the STMAG system have been computed for single FLT images (in units of electrons), we need to "divide" all *PSF magnitudes* derived from the *modified MultiDrizzled* image, MAG_{modDRZ}(PSF) in ADU, by the gain of the CCD.

$$MAG_{FLT}(PSF) = MAG_{modDRZ}(PSF) - 2.5\ \log(gain_{ccd}). \quad (2)$$

We then select 10–20 uncrowded and bright (*F606W* and *F814W* magnitudes brighter than 16.5 mag and 15.5 mag, respectively) stars on the *MultiDrizzled* image and measure their total magnitudes inside a radius of 18.5 pix, $MAG_{modDRZ}(18.5)$, using PHOT in DAOPHOT. Since this magnitude value will be that corresponding to the *modified MultiDrizzle* image (whose flux is in ADU), we need to convert it into magnitudes on the FLT image (whose flux is in electrons).

$$MAG_{FLT}(18.5) = MAG_{modDRZ}(18.5) - 2.5\ \log(gain_{ccd}). \quad (3)$$

For each image, we calculate the mean value of the difference between these two magnitudes. The mean value of this difference is the aperture correction, AP_CORR(18.5), for each FLT image. This value is then added to all of the PSF magnitudes of the FLT image, MAG_{FLT}(PSF). The resulting magnitudes, MAG_{apcorr}, need to be converted from this "intermediate" aperture to "infinity" or *observed magnitude*, $OBMAG_{FLTinf}$. This is done using equation (2) in Sirianni et al. (2005). Strictly speaking, the Sirianni et al. corrections to infinity are only applicable to the drizzled images, not the FLT images. Nevertheless, in a recent paper, Sarajedini et al. (2006) show that there is no significant difference between them. In order to use this equation, MAG_{apcorr} needs to be set to COUNT_RATE in electrons s^{-1} through the following equation

$$\text{COUNT\_RATE (electrons s}^{-1}) = \frac{10^{MAG_{apcorr}(18.5)/2.5}}{t_{exp}}. \quad (4)$$

Once all magnitudes have been set to the *observed magnitude*, $OBMAG_{FLTinf}$, they need to be corrected by the CTE correction previously computed. The $OBMAG_{final}$ will be used to transform the instrumental magnitude system to the STMAG system following Eq. (7) of Sirianni et al. (2005).

3.3. Conversion to STMAG absolute magnitudes

Finally the observed STMAG magnitudes need to be converted into absolute STMAG magnitudes taking into account the distance at which the clusters lie and their reddening value. This was done following the procedure by Brown et al. (2005). A value of $(m-M)_0 = 24.43$ (Freedman & Madore 1990) was used for the true distance modulus. For each cluster, two reddening values were considered: 0.1 and 0.23 The value $E(B-V) = 0.1$ is the Milky Way line of sight reddening in the direction of M 31. It is the value estimated for G280 by Frogel et al. (1980). $E(B-V) = 0.23$ is the value estimated for G78 by Jablonka et al. (1992). There is no reddening value in the literature for G213.

4. Statistical selection of stars

Since we are interested in determining the width of the RGB of each cluster, we need to eliminate any spurious photometric detections that might contaminate our results. In order to do so, stars were statistically selected to eliminate objects with dubious values for the error, χ^2 and sharpness. This was done prior to the photometric calibration, that is, with the star magnitudes given in instrumental magnitudes. Figures 3–5 show the output of DAOPHOT for the total ACS field of the three clusters. For all three parameters, most points seem to follow a global trend. For instance, in the case of G280, error values increase from ∼0.02 at 16.0 *F814W* to 0.4 at 22.0 *F814W*. There is however, a percentage of outliers for each distribution for all magnitude values. We considered these points as possible spurious photometric detections to be removed before any analysis. A statistical selection was done on the estimate of the dispersion and the mean value of the distribution of each parameter. The mean value of the distribution was computed recursively; after each computation, stars beyond 3 sigma of the distribution were eliminated before the next computation of the mean. A bin of 0.7 mag was used for parameters in the *F606W* filter and a bin of 0.5 mag in the *F814W* filter. The computation of the mean was performed until the difference between subsequent values of the mean value of

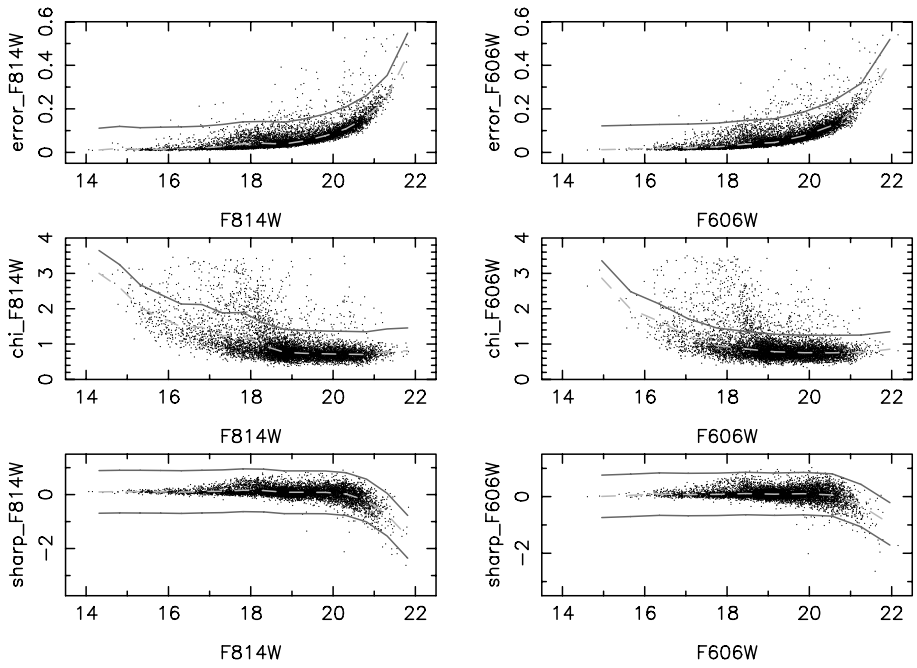

Fig. 3. DAOPHOT/ALLSTAR output for G78. *Top*: error vs. magnitude for both *F606W* and *F814W* instrumental magnitudes. *Middle*: χ^2 vs. magnitude. *Bottom*: sharpness vs. magnitude. Solid lines show the upper limits for stars used to build the CMDs of the cluster and the field; dashed line shows the averaged value after iteration. In the case of the sharpness a lower limit was also used to select stars.

each parameter became lower than 1% of the value. Once this final mean value was determined, we considered the highest value of the dispersion of each parameter (since the computation was done independently for each magnitude bin the dispersion values vary from one bin to the other). This value for the dispersion was multiplied by a factor between 1.0 and 3.5 in order to delimit the edges of the distribution. These factors were chosen in order to draw the boundaries that follow the bulk of the distribution of each parameter value. The solid lines in Figs. 3–5 show the upper limit for the statistical selection of stars; the lower limit for the selection was also considered in the case of the sharpness. The dashed lines show the average value of each parameter. For all clusters, stars whose χ^2 values were over 3.5 for both filters were discarded before any statistical selection was done, in order to facilitate the statistical selection and to eliminate stars that had undetermined sky flux to be used for the CTE correction.

Following this selection, we were left with 7770 stars from the initial 8139 stars for G78. For G213, 13 275 stars from 14 781 initial stars were selected. For G280, 11 204 stars from 12 409 were kept. The remaining stars are identified with a value of 1 in Col. (12) of Table 2[4].

5. Artificial stars experiments

To evaluate the photometry extraction and to quantify the effects of stellar crowding, we performed ten sets of artificial star experiments per cluster. These were done using instrumental magnitudes. In order to do so, we constructed the CMD of each cluster in instrumental magnitudes. Left panels of Fig. 6 show the CMD derived for each cluster, right panels show the CMD built considering all the stars in the ACS FoV – after statistical selection. For the cluster CMDs, stars were selected within a circle centered on each cluster. This was done through the analysis of the radial distribution of stars on each FoV. Figure 7 shows the radial density profile for the entire FoV centered on each cluster. The outer radius of the cluster, $R_{\rm out}$, was chosen to be the radius at which the density profile dropped significantly before reaching a fairly constant value in order to minimize contamination from field stars. This plateau is assumed to represent the density of the surrounding field. Values for $R_{\rm out}$ are shown in Table 5. We then derived the fiducial RGB for each cluster by fitting the mean locii of stars between 15.8 and 18.2 mag in the *F814W* filter. The faintest limit of the magnitude interval was chosen to avoid the mixed stellar population of the red clump.

For each experiment, we selected 384 stars along the fiducial RGB of each cluster from 15.8 to 18.2 in *F814W* in magnitude bins of 0.05 to fully cover the RGB interval. This resulted in 8 stars per magnitude bin per experiment and 80 stars per magnitude bin for the ten experiments as a whole – in total, 9216 artificial stars were used for the experiments. The artificial stars were added to both the *F606W* and *F814W* HRC/ACS *MultiDrizzled* frames with the constraint that no two artificial stars be within 1.5 PSF radii of each other and avoiding the edges of the images. The number of artificial stars considered per experiment was chosen to be small enough to avoid introducing important density variations in the FoV of the clusters. The number of artificial stars introduced in the FoV is at most 5% of the total number of real stars in the field. The photometry from the resultant images was computed following the exact same steps used to derive the photometry of the observed images (see Sect. 3.1). The percentage of recovered stars for all ten experiments per cluster is 97.94%, 98.13% and 98.29% for G78, G213 and G280, respectively. The missing fraction are artificial stars whose photometry could not be extracted with DAOPHOT because they are located too close (<3 px) to real stars in the FoV.

Figure 8 displays the input artificial stars along the fiducial RGB and the recovered RGB stars for all the experiments in each cluster. No statistical selection of output stars was done for this comparison. For the three clusters, the input sequence is well

[4] The complete individual photometric measurements for each cluster are only available in electronic form at the CDS.

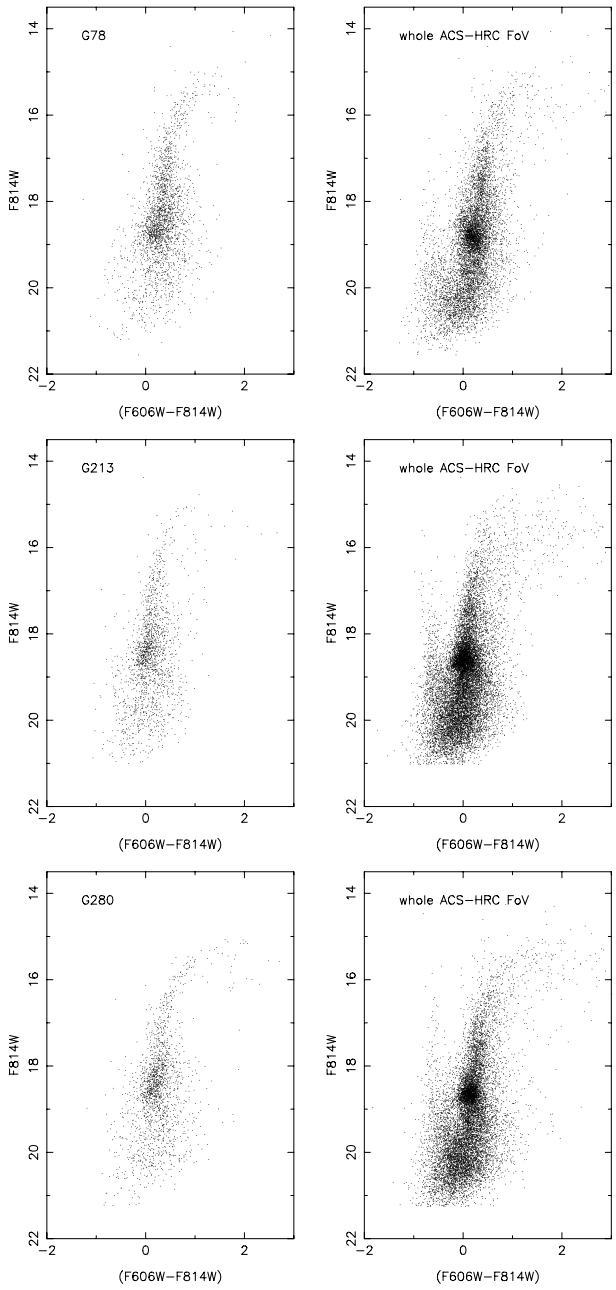

Fig. 6. *Left panels*: color−magnitude diagrams (CMD) for G78 (*top*), G213 (*middle*) and G280 (*bottom*) considering all stars within R_{out} – values given in Table 3. *Right panels*: CMDs considering all the stars in the field of view (FoV) of the *MultiDrizzled* HST-ACS images of G78 (*top*), G213 (*middle*) and G280 (*bottom*).

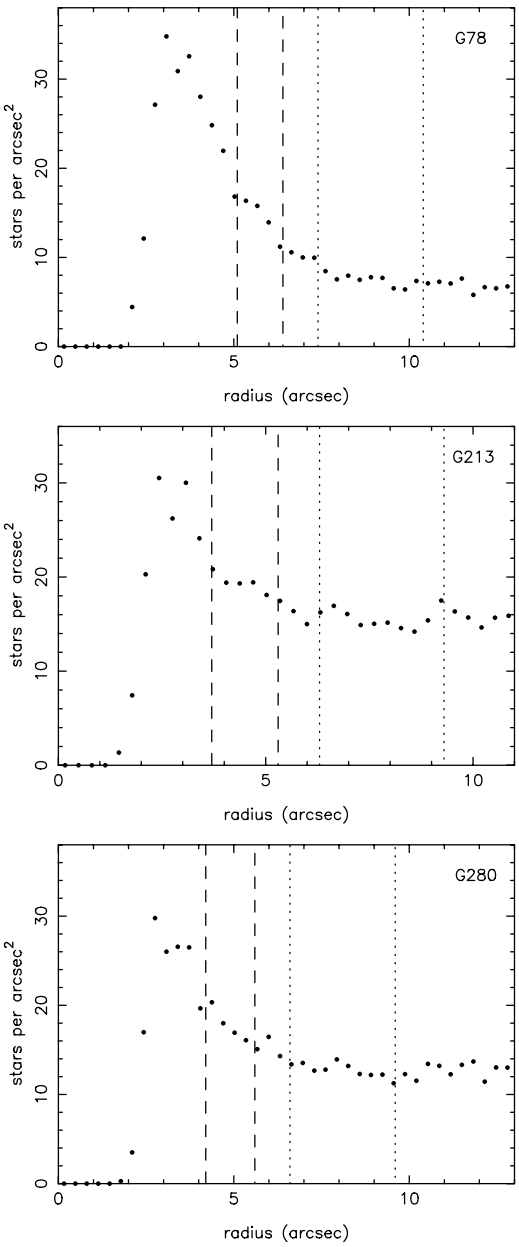

Fig. 7. Density profile for all stars in the FoV of G78 (*top*), G213 (*middle*) and G280 (*bottom*) after statistical selection (see Sect. 4). Dashed lines delimit the region used to construct the CMD of each cluster. Dot-dashed lines delimit the region of the FoV used for the CMD of the surrounding stars (see Sect. 7.2). Apparent density holes near the center of the clusters are due to star crowding.

recovered. Less than 5.0% of recovered stars fall below the magnitude 18.2 in *F814W* – for G78 it is less than 2.5%. For this same cluster, less than 1.0 % of the recovered stars fall to the right (and/or left) of the fiducial RGB – between 1 and 2 mag in color. The same occurs for the recovered stars of G280. For G213, there is a higher percentage of stars (~3.0%) falling outside the "main" body of the RGB than for G78 and G280. This is probably due to the fact that the FoV of this cluster is more populated than those of G78 and G280. In all cases, the number of outliers from the recovered RGB is small. These are stars whose recovered magnitudes differ significantly from the input magnitudes because they happen to overlap with the original (real) stars in the FoV. Although the artificial stars were placed so that no two artificial stars are within 1.5 PSF radii of each other, no such restriction was imposed for stars already in the FoV.

An evaluation of the input minus the recovered magnitudes in the *F606W* and *F814W* filters according to the position of the star from the center of the cluster showed that this difference increases at small radii ($R \sim 4.8'', 3.5''$ and $4.0''$ for G78, G213 and G280, respectively) introducing an artificial brightening for stars near the center of each cluster. Figure 9 shows the difference between the input magnitudes of the artificial stars and their recovered magnitudes (mag_diff) according to their radial position with respect to the center of each cluster. An important departure from zero is seen for low values of R. For higher values, some stars do "migrate" in magnitude, but they are few if compared to the bulk of the stars which fall around zero. In

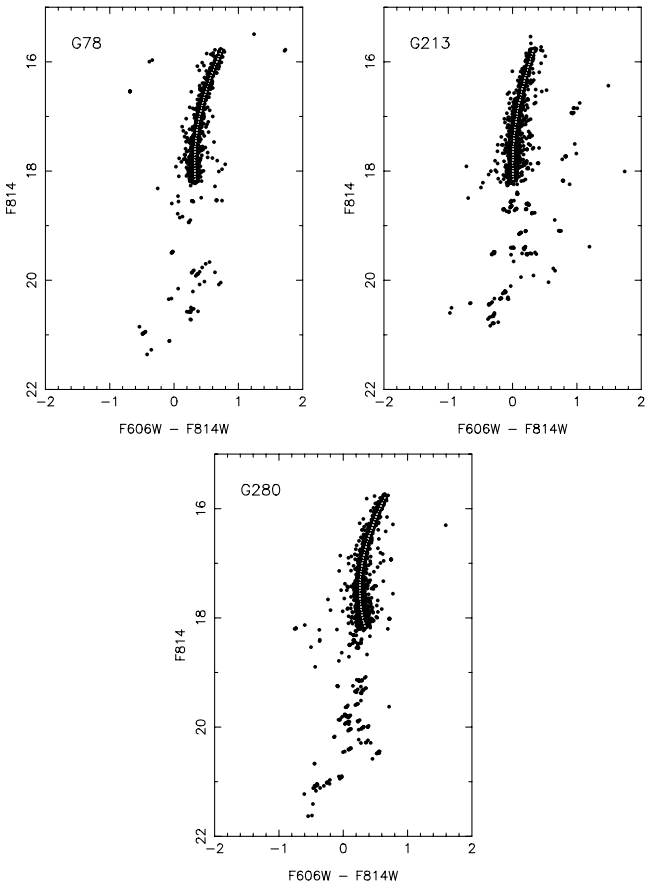

Fig. 8. Results of the artificial stars experiments with no statistical selection of stars for G78 (*top left*), G213 (*top right*) and G280 (*bottom*). The thin white solid line indicates the input RGB while the dots indicate the output (measured) RGB stars.

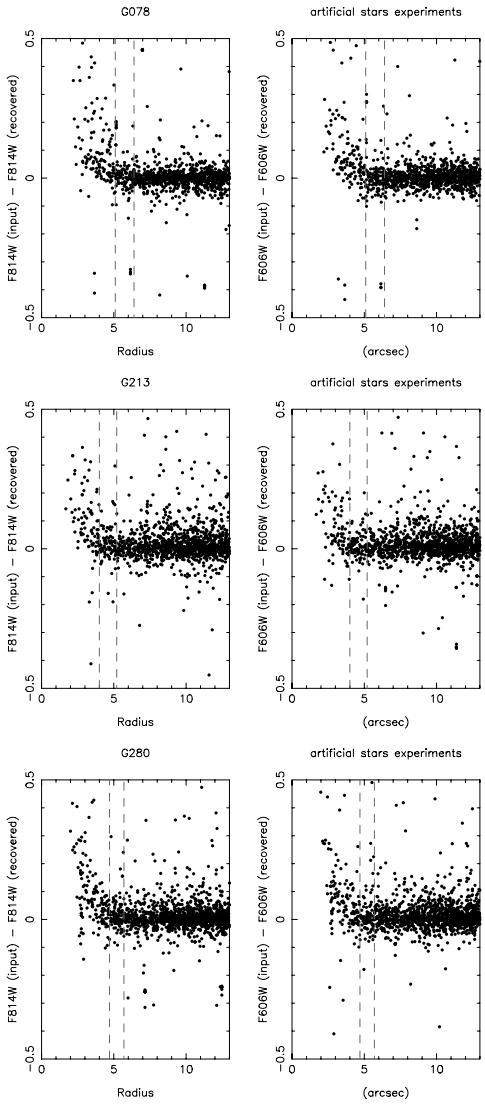

Fig. 9. Input and recovered magnitude difference according to radial position for G78 (*top*), G213 (*middle*) and G280 (*bottom*). For each cluster, the inner lines correspond to 5.1″, 3.7″ and 4.2″ for G78, G213 and G280, respectively, while the outer lines correpond to 6.4″, 5.3″ and 5.6″ for G78, G213 and G280, respectively.

order to evaluate this brightening for the stars in each cluster, we computed the average value of mag_diff and its dispersion within $R_{\rm out}$. We considered all stars within an annulus of outer radius $R_{\rm out}$ and whose inner radius we varied until the absolute average value of mag_diff was less than 0.02 mag and the dispersion value was close to 0.05 mag or less. Results are shown in Table 3. This final radius was set to be the inner radius $R_{\rm in}$ of the cluster. All stars lying within this radius will not be taken into account in the analysis that follows.

Sources of error, e.g., such as residual flat-field non-uniformities and residual dark current, are not included in our photometric error estimates. However, those should not dramatically increase our estimates. There is also a possibility that small differences exist between the PSF model used in the artificial star experiments and the profiles of the real stars. This source of error is difficult to quantify; however, we believe it is likely to be negligible because of the spatial resolution of the ACS/HRC instrument which provides good sampling of the PSF (*FWHM* ∼ 3 pixels).

6. Luminosity function

The luminosity function (LF) for each cluster and its surrounding field stars was derived using a bin of 0.15 in magnitude[5]. Field stars were selected within a concentric annulus with an inner radius 1.0″ larger than the outer radius of the cluster, $R_{\rm out}$ – defined in Sect. 5. This was done to reduce the number of cluster stars that could be contaminating the field. The outer radius of the ring containing field stars was chosen 3.0″ larger than its inner radius. The LF of each cluster was computed considering all of the stars between the inner radius, $R_{\rm in}$ and outer radius, $R_{\rm out}$ defined in the previous section. Figure 10 shows the luminosity function for each cluster and its corresponding surrounding field. Figure 11 shows the resulting luminosity function of each cluster subtracted from the contribution of the stars in the surrounding field. For G78, an $E(B-V)$ of 0.23 was considered initially (taken from Jablonka et al. 1992). This value was then changed to 0.22 in order to match the location (in magnitude) of the HB of G78 to the location (in magnitude) of the HBs of G213 and G280. For G280, $E(B-V) = 0.1$ (Frogel et al. 1980). For G213, there are no reddening values in the literature, so the luminosity function was computed considering $E(B-V) = 0.1$, which is taken to be the standard value along the M 31 line of sight. The superposition of the CMD of G213 with the standard

[5] Absolute STMAG magnitudes are considered from this part of the analysis onwards.

Table 3. Average value and dispersion of the difference between the input magnitude and recovered magnitude between specific radial intervals for each cluster.

Cluster	radial interval (″)	mean magnitude difference	dispersion
G78	5.1–6.4	–0.0203	0.0454
G213	3.7–5.3	0.0343	0.0551
G280	4.2–5.6	0.0425	0.0528

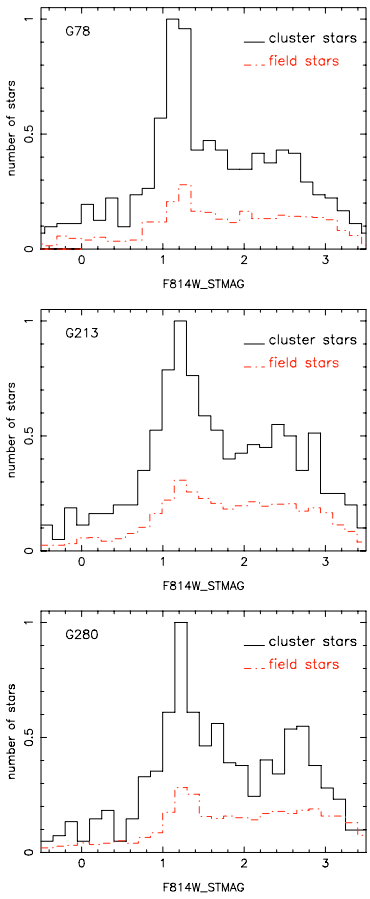

Fig. 10. Luminosity function (LF) for G78 (*top*), G213 (*middle*) and G280 (*bottom*) and their corresponding surrounding fields. For each cluster, the LF was derived considering the following inner radii, $R_{\rm in}$ = 5.1″, 3.7″, 4.2 ″ for G78, G213 and G280 respectively.

RGB of sequences of Brown et al. (2005) confirms the validity of this choice (middle panel of Fig. 12). For each cluster and its surrounding field, the red clump lies at ∼1.185.

7. RGB width determination

7.1. Final CMD

The final CMD of each cluster was built considering only statistically selected stars within the ring between $R_{\rm in}$ and $R_{\rm out}$. Figure 12 shows the superposition of the standard RGB sequences and HB loci derived by Brown et al. (2005) on the CMD of G78, G213 and G280. The straight dotted line shows the position of the red clump of each cluster. For the three clusters, the red clump falls at the same position as the HB loci of Brown et al. (2005).

At this point, the CMD of each cluster should be largely free of spurious detections. Nevertheless it will still be affected by the presence of field stars falling within the area of each cluster.

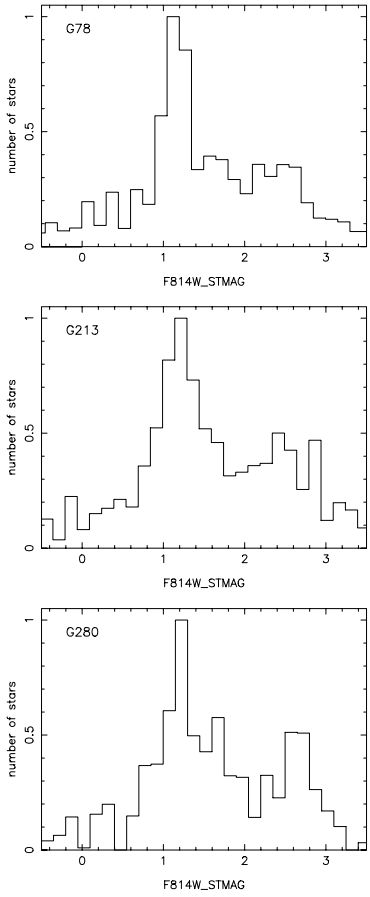

Fig. 11. Luminosity function (LF) for G78 (*top*), G213 (*middle*) and G280 (*bottom*) subtracted from the contribution of their corresponding surrounding fields.

In order to estimate the contribution of field stars to the RGB of each cluster, we also constructed the CMD of the stars in the surrounding fields. These stars were chosen within the outer annulii described in Sect. 6. The left panels of Fig. 13 show the CMDs of G78, G213 and G280. Right panels of the same figures show the CMD of their corresponding surrounding fields.

For the final CMD of each cluster, the fiducial RGB was derived by fitting the mean locii for stars within certain magnitude and color intervals. The upper magnitude limit was set at 0.5 mag brighter than the position of the red clump. The lower magnitude limit, as well as the color limits, were set in order to get rid of obvious outliers of the RGB. Magnitude and color intervals for each cluster are shown in Table 4. The fit is shown in Figs. 12 and 13. The dark lines in the left panels of these figures show the mean locii of the RGB regions of each cluster.

7.2. Density distribution of fields stars vs. cluster stars

In order to determine the actual contribution of field stars to the RGB of the cluster, we need to compare the density distribution of field stars to that of stars in the cluster. Figure 7 shows the density distribution of the clusters and their surrounding field. Since the cluster stars have been selected in view of the robustness of their photometry, the most central stars of the cluster are missing. This leaves a hole in the radial distribution of stars. The average density of stars in each annulus (associated to each cluster and to its surrounding field), as well as the surface of the cluster are given in Table 5.

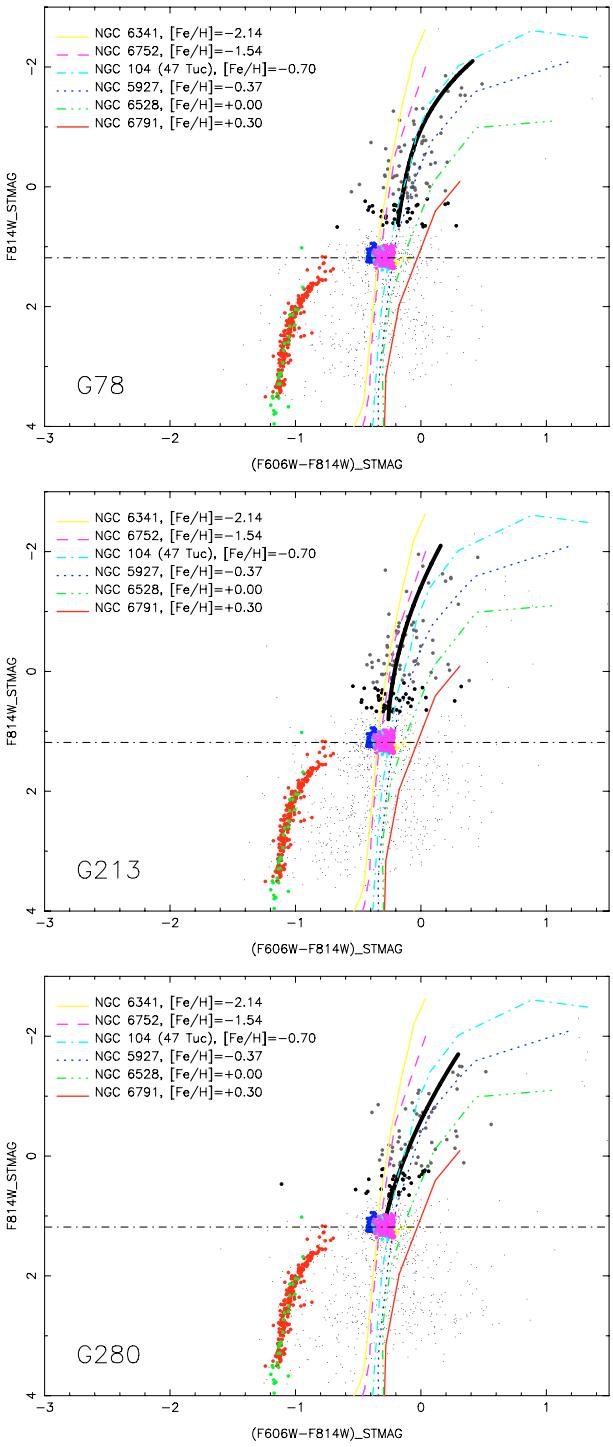

Fig. 12. Superposition of the ridges and HB loci derived by Brown et al. (2005) on the CMD of G78 (*top*), G213 (*middle*) and G280 (*bottom*). Thick solid line indicates the position of the fiducial RGB of each cluster. The straight dotted line shows the position of the red clump of each cluster.

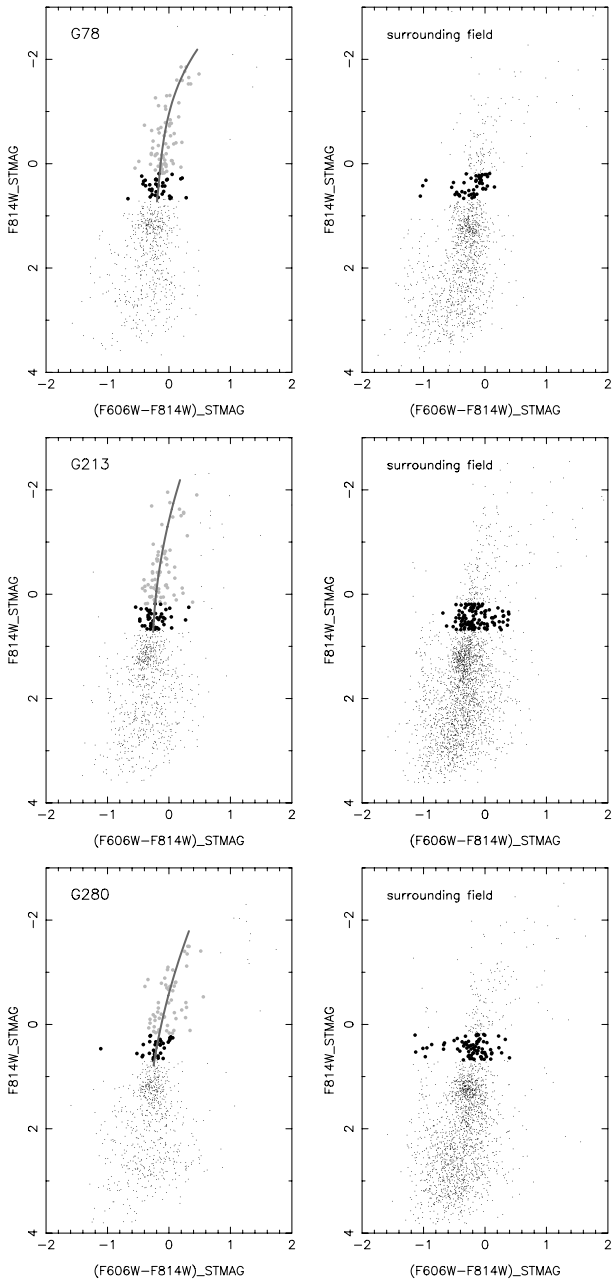

Fig. 13. Color−magnitude diagrams (CMD) for G78 (*top left*), G213 (*middle left*) and G280 (*bottom left*) and corresponding surrounding fields, *top right* for G78, *middle right* for G213 and *bottom right* for G280. Grey dots indicate the stars considered for the fit of the RGB. Solid lines show the locus of this fiducial RGB. Black dots indicate the stars considered for computation of the RGB width. Right panels show the CMD for each surrounding region. Dark dots indicate stars considered for the analysis of the contribution of field stars to the width of the RGB of the cluster.

7.3. Color difference histograms for clusters and surrounding fields

Figure 14 shows the color difference histograms around the fiducial RGB for each cluster and its corresponding field. These histograms show the difference between the color of a star with a certain magnitude and the color value of the fiducial RGB at the same magnitude. RGB stars were considered within a magnitude interval of 0.5 mag, with its faintest limit set at 0.5 mag above the red clump. This value was chosen to avoid the mixed stellar population of the red clump, while the brighter limit of the magnitude interval (0.5 mag brighter) was chosen to avoid the upper parts of the RGB that could be polluted by AGB stars. The magnitude interval for the three clusters goes from 0.185 to 0.685 mag. Histograms were derived using a color bin of 0.085 mag for G78 and G213 and 0.090 mag for G280. The size of color bin was chosen to best sample the distribution of stars along this part of the RGB according to each cluster. The

Table 4. Magnitude and color values for the boundaries of the intervals considered to fit the RGB of each cluster.

Cluster	lower mag	upper mag	lower color	upper color
G78	−2.2	0.685	none	0.8
G213	−2.2	0.685	−0.7	0.5
G280	−1.8	0.685	none	0.6

distribution of the field stars was scaled to the same area as the cluster stars based on the values of R_{in} and R_{out} shown in Table 5. Histograms were obtained by direct bining of stars per unit color (straight line histograms in Fig. 14). So-called "generalized histograms" (filled circles in the same figure) were obtained by weighting the contribution of each star to each color bin of the histogram with its photometric error, i.e. the value of the photometric error of each star, determined the weight this star would add to the star counts in each color bin of the histogram. For all three clusters, the first histogram (simple histogram) and the second one (*generalized* histogram) follow the same trend. Once the color distributions of the field stars had been properly scaled to the area considered for the determination of the color distribution of the cluster stars, the field stars were directly subtracted from the cluster stars per color and magnitude bin in order to derive a color distribution of cluster stars along the RGB.

8. Analysis of RGB width

In order to evaluate the contribution of photometric errors to the width of each cluster's RGB, we derived the CMD of the recovered artificial stars after applying a similar statistical selection than the one done for the observed stars and described in Sect. 4, as well as using the magnitude and color limits shown in Table 4. Only artificial stars falling within each cluster annulus are considered. Figure 15 shows the CMD of these artificial stars.

Considering the same magnitude intervals than the ones used in the previous section to compute the color histograms of the observed stars, we derived the color histogram of the recovered artificial stars. Empty circles in Fig. 16 show the generalized normalized histogram of the recovered artificial stars per cluster. The dashed line shows the Gaussian fit. Filled circles in the same figures display the generalized normalized histogram for the observed stars without the contribution of field stars. Solid lines show the Gaussian fits. The resulting histograms for the observed stars are not centered on zero due to the fact that the fiducial RGB was derived before the subtraction of field stars, i.e., considering both cluster and field stars. Once the subtraction was done, the locus of the remaining distribution is slightly shifted from zero. For G78, there is a shift of −0.03 mag; for G213, the shift equals −0.03 mag; for G280, there is a shift of 0.02 mag. Rows 6 and 7 of Table 5 display the values of σ for the two Gaussian fits along with their uncertainties. σ_{obs} corresponds to the distribution of observed stars while σ_{art} corresponds to that of the artificial stars. These values were subtracted in quadrature in order to analyze the intrinsic width of the observed stars distribution for each cluster. The last row of Table 5 show the resulting difference, $\sigma_{int} = (\sigma^2_{obs} - \sigma^2_{art})^{1/2}$ and its uncertainty.

9. Determination of the color-metallicity relation and metallicity dispersion

Assuming the intrinsic color width of the RGB of these clusters is due entirely to a metallicity dispersion, we can estimate the value of this dispersion by constructing the color-metallicity relation using the standard RGB sequences of Brown et al. (2005). Considering the central magnitude of the interval used to estimate the intrinsic color width of the clusters, we plotted the corresponding color values for each standard RGB sequence in Brown et al. (2005) versus its metallicity. These points were fitted using a second order polynomial in order to derive the color-metallicity relation for the clusters as shown in Fig. 17. The resulting color-metallicity relation for the three clusters is:

$$[\mathrm{Fe/H}] = 0.0952 + 2.8323(V-I)_0 - 12.5153(V-I)_0^2 \quad (5)$$

where $(V-I)_0$ is the RGB color at $I = 0.435$ mag, which is 0.75 mag brighter than the HB. Using this expression, we derived a metallicity dispersion for each cluster.

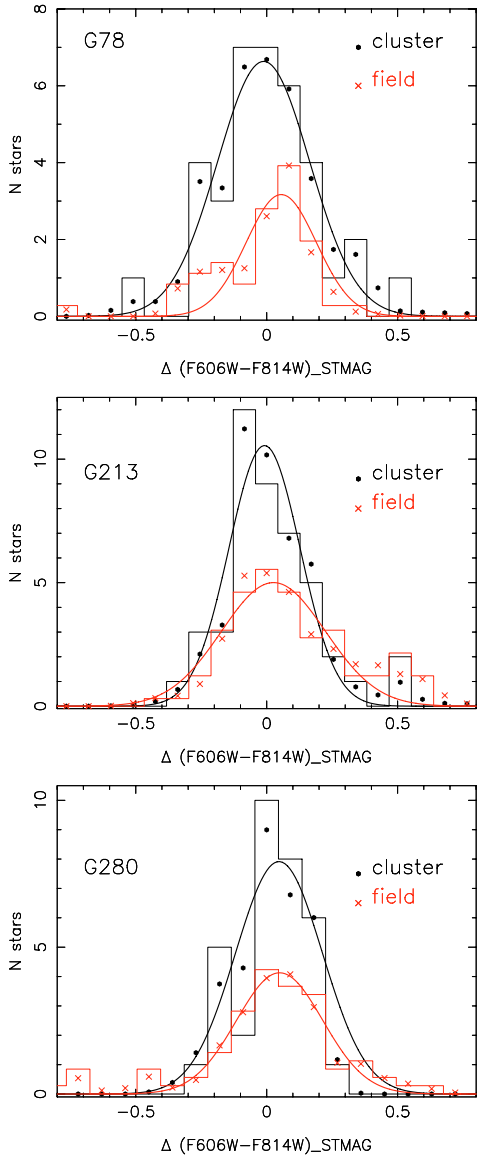

Fig. 14. Color histograms for each cluster, G78 (*top*), G213 (*middle*) and G280 (*bottom*), and its corresponding surrounding fields. Solid straight lines show the simple histogram of both the cluster and the surrounding field derived by simple bining of stars per color interval. Dots (for the cluster) and crosses (for the surrounding field stars) display the histograms obtained by weighting the contribution of each star to each color bin with its associated photometric error. Solid lines indicate the Gaussian fit for each case.

Table 5. Parameters for the RGB width analysis and sigma values from the Gaussian fits of color distributions of observed and artificial stars.

Cluster ID	G78	G213	G280
R_{in}(arcsec)	5.1	3.7	4.2
R_{out}(arcsec)v	6.4	5.3	5.6
Cluster density (stars per arcsec^2)	14	20	19
Field density (stars per arcsec^2)	7	15	12
Cluster surface (arcsec^2)	55	45	43
$\sigma_{obs} \pm \Delta\sigma_{obs}$	0.1449 ± 0.0395	0.1110 ± 0.0261	0.1439 ± 0.0415
$\sigma_{art} \pm \Delta\sigma_{art}$	0.0587 ± 0.0142	0.0472 ± 0.0085	0.0566 ± 0.0129
$\sigma_{int} \pm \Delta\sigma_{int}$	0.1325 ± 0.0397	0.1005 ± 0.0261	0.1323 ± 0.0416

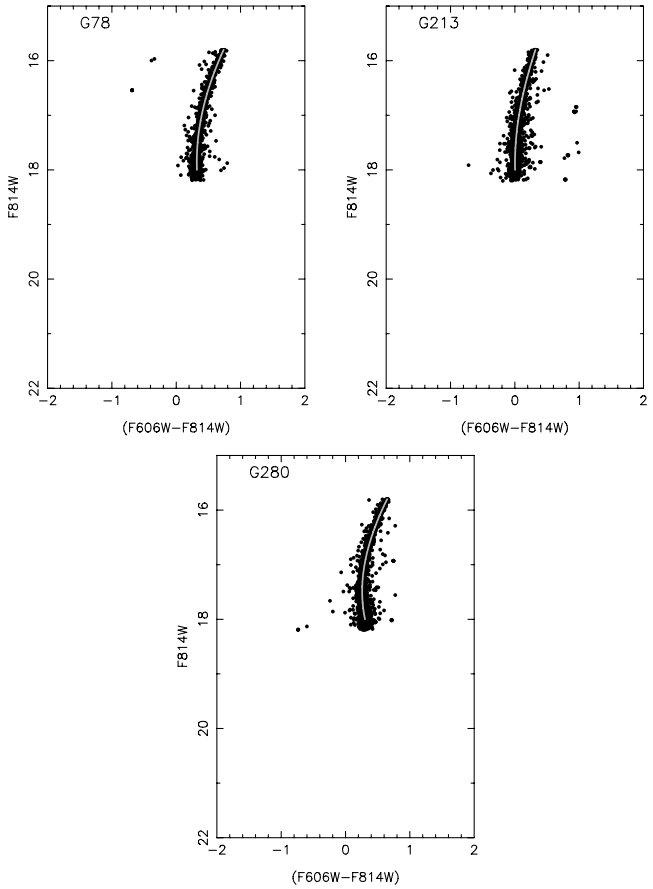

Fig. 15. Results of the artificial star experiments after applying the statistical selection of stars described in section 4 for G78 (*top left*), G213 (*top right*) and G280 (*bottom*). The solid line indicates the input RGB while the dots indicate the output (measured) RGB stars. Only stars falling within each cluster annulus were considered.

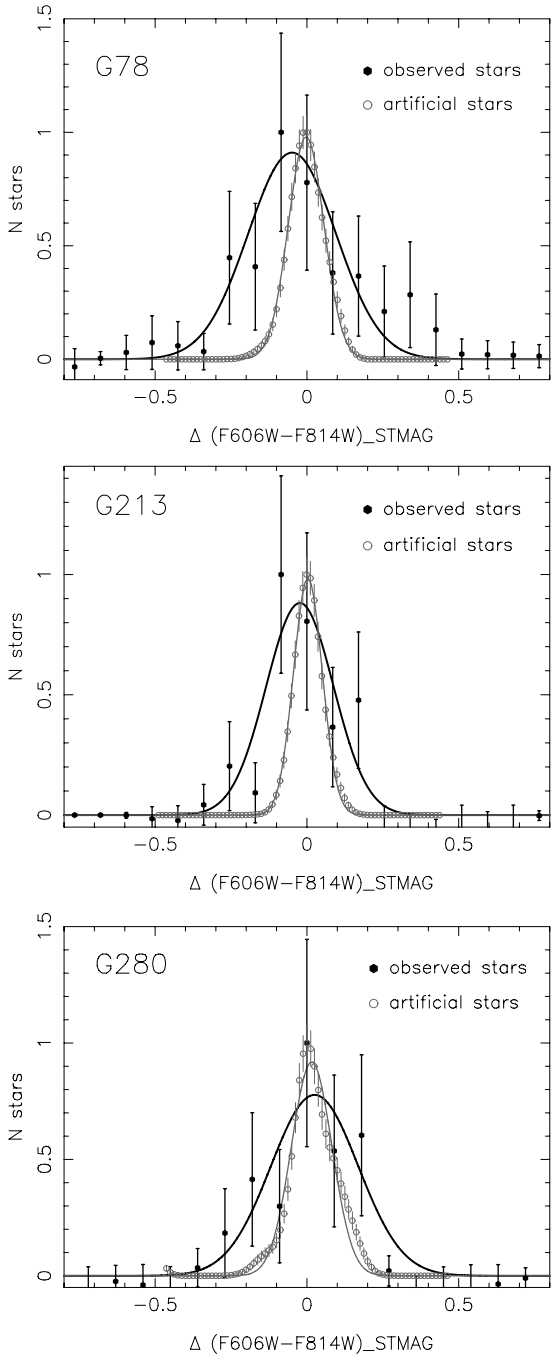

Fig. 16. Resulting color histogram for G78 (*top*), G213 (*middle*) and G280 (*bottom*). Filled dots display the color distribution of observed stars. Empty circles display the color distribution of recovered artificial stars. Solid and dashed lines showed the fitted Gaussians for each case.

First we compute the metallicity for the color $(V-I)_0$, which we shall call [Fe/H]$_0$. Then we add to $(V-I)_0$ the intrinsic color dispersion computed from the histogram fit in Sect. 8, that is σ_{int}, to have $(V-I)_0+\sigma_{int}$. This value is inserted into Eq. (1) to derive the "upper limit" of the metallicity dispersion, [Fe/H]$_{up}$. For the "lower limit" of the metallicity dispersion, we subtract to $(V-I)_0$ the intrinsic color width, that is $(V-I)_0-\sigma_{int}$, and insert this value into the [Fe/H] vs. color relation to obtain [Fe/H]$_{low}$. These lower and upper limit are indicated with crosses in Fig. 17. The metallicity dispersion will be given by ([Fe/H]$_{up}$ − [Fe/H]$_{low}$)/2 even though [Fe/H]$_0$ does not lie in the middle of this interval. The metallicity dispersion of each cluster is given in Table 6. We give both the resulting dispersion and the relative dispersion, $\sigma_{[Fe/H]}$/[Fe/H], where [Fe/H] is given in Table 1.

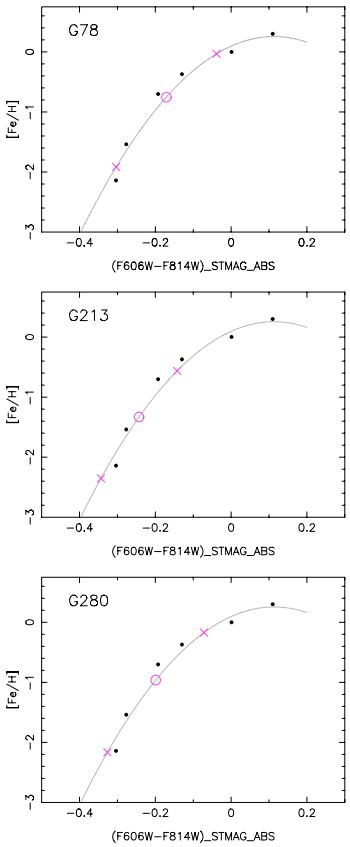

Fig. 17. Color versus metallicity plot for a magnitude value of $F814W = 0.435$ derived from the Brown et al. (2005) ridgelines. Solid line shows the fit of second order polynomial given by Eq. (1). Empty circle shows the position of the RGB of G78 at that magnitude value considering $E(B-V) = 0.22$ (*top left panel*); empty circle shows the position of the RGB of G213 at that magnitude value considering a reddening of 0.1 (*top right panel*); empty circle shows the position of the RGB of G280 at that magnitude value considering a reddening of 0.1 (*bottom panel*). For all three panels, crosses indicate the lower and upper limits in color and metallicity used to determine the metallicity dispersion of each cluster.

Table 6. Metallicity dispersion for each cluster.

Cluster ID	G78	G213	G280
$\sigma_{[Fe/H]}$	0.9419	0.8955	1.0337
error	±0.3824	±0.1979	±0.2587
$\sigma_{[Fe/H]}$/[Fe/H]	1.0238	0.8292	1.4767
error	±0.4157	±0.1832	±0.3695

As mentioned in Sect. 5, we have performed the photometry and the artificial stars experiments with great care. The latter have been conducted in such a way as to include all known sources of photometric error that are readily quantified. Nonetheless, there is a small chance that we have underestimated the actual photometric errors, in which case, our inferred cluster metallicity dispersions would be upper limits of the true values.

As a comparison, the intrinsic metallicity dispersion of G1 ($\sigma = 25.1$ km s−1, [Fe/H] = −1.08) is ±0.5 dex for $E(B-V) = 0.10$, and ±0.39 dex for $E(B-V) = 0.05$ (Meylan et al. 2001), which is equivalent to that of the three clusters within the error bars. We note that the G280's metallicity dispersion that we derive in this work is much higher than the value found by (Stephens et al. 2001) in their study involving NICMOS observations of metal-rich globular clusters in M 31. According to those authors, $\sigma_{[Fe/H]} \sim 0.2$, using the dispersion in the measured $(J-H)$ and $(J-K)$ colors. This difference is probably due to the fact that for any spread in [Fe/H], the corresponding spread in color is twice as small in the infrared $(J-K)$ than in the visible $(V-I)$. Also the fact that they work with a smaller sample (∼200 stars versus ∼2500 stars per cluster in this work) would statistically affect their measurement of any spread in metallicity.

10. Discussion and conclusions

In light of the existing hypotheses made for the case of our Galaxy, we now consider some possible explanations for the metallicity dispersion seen in the four most massive globular clusters in M 31.

In a scenario of chemical self-enrichment, the cluster metallicity dispersion comes from stars originating from the gas trapped in the globular cluster after its formation. Therefore, one expects a more massive cluster to retain more gas and thus to exhibit a more prominent contribution from the second generation of stars. In our case, the metallicity dispersions of the three clusters are similar within the error bars. On the other hand, if their velocity dispersions are directly linked to their masses, G78 and G280 have similar masses, while G213 is less massive. With this information, we are not able to establish any link between the metallicity dispersion and the mass of the clusters. This lack of a correlation between the cluster metallicity dispersion and velocity dispersion could indicate that the role of the cluster mass in widening its RGB is not straight-forward. However it is hard to draw any conclusion from such a small sample of clusters.

A second attractive explanation for the observed width of the RGB of these clusters would be that they are actually the remains of tidally stripped dwarf galaxies. Recent results on dwarf-globular transition objects (DGTOs – Hasegan et al. 2005) and ultra-compact dwarf (UCD) galaxies in Virgo (Jones et al. 2006) and Fornax (Drinkwater et al. 2003) support the hypothesis that these objects are the remnant nuclei of threshed dE,N galaxies. Zinnecker et al. (1988) and Freeman (1993) have already suggested the possibility of ω Cen being the remaining core of a larger entity such as a former nucleated dwarf elliptical galaxy. Bekki & Freeman (2003) suggest that the thick disk of our Galaxy might have been formed by the accretion of dwarf spheroidals such as ωCen. The results of Meylan et al. (2001) on G1 indicate this cluster could be a kind of transition step between globular clusters and dwarf elliptical galaxies, being the remaining core of a dwarf galaxy whose envelope would have been severely pruned by tidal shocking due to the bulge and disk of its host galaxy, M 31. Considering that M 31 also possesses a thick disk (Sarajedini & Van Duyne 2001) and seems to have suffered more tidal stripping events than the MW (Ibata et al. 2001; Brown et al. 2006), one would expect the presence of other remaining cores as "relics" of the history of interactions of this galaxy resembling the clusters studied in this work. In fact, both G213 and G280 seem to fall (at least in projection) on one of the trajectories suggested by Ibata et al. (2004) for the passage of a satellite galaxy that might have been tidally disrupted by M 31.

In order to explore this idea, we searched for any tidal features (tails or asymmetric envelopes) around the clusters. We looked for any density enhancements in the outer parts of each cluster to the edges of the FoV. For all three clusters there is no clear density excess in any particular direction that could indicate the presence of any tidal feature. However this visible absence of density enhancement is not conclusive, since at

the distance of M 31, it would be difficult to detect any density enhancements from the star-counts of the brighter stars of the cluster – contrary to density enhancement detections in GCs in our Galaxy through star-counting methods including stars on the main sequence (i.e. Grillmair et al. 1995; Lee et al. 2003).

A third possibility would be a primordial metallicity inhomogeneity in the proto-cluster cloud induced by the influence of field stars during the formation of the globular cluster. For a long time the main question was whether these inhomogeneities were inherited at the birth of the stars that we are currently observing (the so-called self-enrichment hypothesis that implies pollution of the intracluster gas by more massive and faster evolving stars) or if they were generated in the course of the evolution of these objects (the so-called evolution hypothesis that requires non-canonical mixing inside the star itself). On the one hand, the classical self-enrichment scenario (Truran et al. 1991; Prantzos & Charbonnel 2006, and references therein) assumes that stars within the GCs created the totality of the metals (light and heavy), and involves three stellar generations. On the other hand, the pre-enrichment scenario (Kraft 1994) assumes that GCs were born with their current heavy metal content and invokes only two stellar generations. Both hypotheses are globally supported by our observations. In order to really be able to have conclusive arguments, we would need detailed chemical information (on α-, r- and s-process elements for example), while the color−magnitude diagnostics only give information on the cluster global metallicities (Z).

In all of the above scenarios, the realm of parameter space for these clusters is large and we are only beginning to explore what the significant metallicity dispersion among their stars might be correlated with. In conclusion, the results presented in this work add to the growing body of evidence that massive globular clusters have a more complex history of star formation and chemical enrichment than would be expected in a traditional view of globular clusters as simple, single-age and single-metallicity stellar systems. Further studies of these and similar objects will likely expand our understanding of galaxy assembly.

Acknowledgements. I.F.C. acknowledges the financial support of FAPESP grant no.03/01625-2 and the Sixth Program of the EU for a Marie Curie Fellowship. AS was partially supported by STScI grant HST-GO-09719.01-A. S.G.D. acknowledges a partial support from the STScI grant HST-GO-09719.03-A, and the Ajax Foundation. I.F.C. also thanks D.R. Gonçalves and H. Flores for computational support.

Note added in proof. Since this paper was accepted for publication, it has been noted that we did not take into account the effect of differential reddening on the width of the cluster RGBs. However, for a number of reasons (e. g. our small field of view, the small absolute reddenings of our clusters), we believe that this effect is likely to be negligible. We thank Ivan King for bringing this to our attention.

References

Barmby, P., Huchra, J. P., Brodie, J. P., et al. 2000, AJ, 119, 727
Bekki, K. 2006, MNRAS, 367, L24
Bekki, K., & Freeman, K. C. 2003, MNRAS, 346, L11
Bekki, K., Campbell, S. W., Lattanzio, J. C., & Norris, J. E. 2007, MNRAS, 377, 335
Brown, T. M., Ferguson, H. C., Smith, E., et al. 2003, ApJ, 592, L17
Brown, T. M., Ferguson, H. C., Smith, E., et al. 2005, ApJ, 1693
Brown, T. M., Smith, E., Ferguson, H. C., et al. 2006, ApJ, 652, 323
Dopita, M. A., & Smith, G. H. 1986, ApJ, 304, 283
Djorgovski, S. G., & Meylan, G. 1994, AJ, 108, 1292
Djorgovski, S. G., Gal, R. R., McCarthy, J. K, et al. 1997, ApJ, 474, L19
Drinkwater, M. J., Gregg, M. D., Hilker, M. J., et al. 2003, Nature, 423, 519
Ferguson, A., Irwin, M., Chapman, S., et al. 2006 [astro-ph/0601121]
Freedman, W. L., & Madore, B. F. 1990, ApJ, 365, 186
Freeman, K. C. 1993, PASP, 48, 608
Frogel, J. A., Persson, S. E., & Cohen, J. G. 1980, ApJ, 240, 785
Gratton, R., Sneden, C., & Carretta, E. 2004, ARA&A, 42, 385
Grillmair, C. J., Freeman, K. C., Irwin, M., & Quinn, P. J. 1995, AJ, 106, 2553
Hasegan, M., Jordán, A., Côté, P., et al. 2005, ApJ, 627, 203
Hilker, M., & Richtler, T. 2000, A&A, 362, 895
Hodge, P. W. 1981, Atlas of the Andromeda Galaxy (University of Washington Press)
Huchra, J. P., Brodie, J. P. & Kent, S. M. 1991, ApJ, 370, 495
Ibata, R., Irwin, M., Lewis, G., Ferguson, A. M. N., & Tanvir, N. 2001, Nature, 412, 49
Ibata, R., Chapman, S., Ferguson, A. M. N., et al. 2004, MNRAS, 351, 117
Ikuta, C., & Arimoto, N. 2000, A&A, 358, 535
Jablonka, P., Alloin, D., & Bica, E. 1992, A&A, 260, 97
Jones, J. B., Drinkwater, M. J., Jurek, R., et al. 2006, AJ, 131, 312
Koekemoer, A. M., Fruchter, A. S., Hook, R., & Hack, W. 2002, HST Calibration Workshop, ed. S. Arribas, A. Koekemoer, & B. Whitmore, 337
Koornef, J., Bohlin, R., Buser, R., Horne, K., & Turnsheck, D. 1986, in Proceedings of the IAU 19th General Assembly, ed. S.-P. Swinggs
Kraft, R. P. 1994, PASP, 106, 553
Lee, Y.-W., Joo, J.-M., Sohn, Y.-J., et al. 1999, Nature, 402, 55
Lee, K. H., Lee, H. M., Fahlman, G. G., & Lee, M. G. 2003, AJ, 126, 815
Meylan, G., Mayor, M., Duquennoy, A., & Dubath, P. 1995, A&A, 303, 761
Meylan, G., Sarajedini, A., Jablonka, P., et al. 2001, AJ, 122, 830
Norris, J. E., & Da Costa, G. S. 1995, ApJ, 447, 680
Prantzos, N., & Charbonnel, C. 2006, A&A, 458, 135
Sarajedini, A., & Van Duyne, J. 2001, AJ, 122, 2444
Sarajedini, A., Barker, M. K., Geisler, D., Harding, P., & Schommer, R. 2006, AJ, 132, 1361
Sirianni, M., Jee, M. J., Benitez, N., et al. 2005, PASP, 117, 1049
Smith, G. H., & McClure, R. D. 1987, ApJ, 316, 206
Stephens, A. W., Frogel, J. A., Freedman, W., et al. 2001, AJ, 121, 2597
Stetson, P. B. 1994, PASP, 106, 250
Tsujimoto, T., & Shigeyama, T. 2003, ApJ, 590, 803
Truran, J. W., Brown, J., & Burkert, A. 1991, ASPC, 13, 78
Zinnecker, H., Keable, C. J., Dunlop, J. S., Cannon, R. D., & Griffiths, W. K. 1988, IAUS, 126, 603

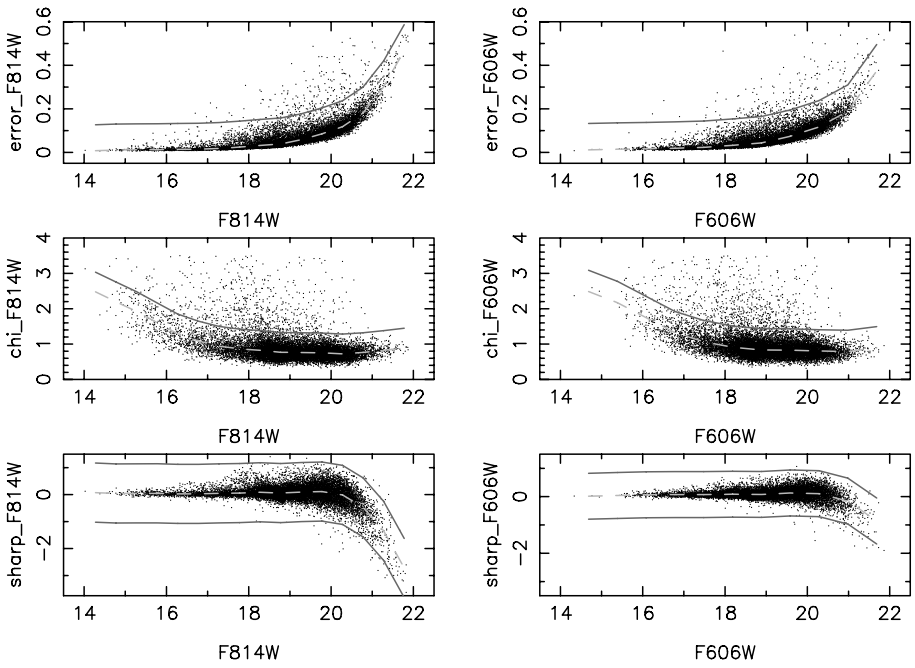

Fig. 4. DAOPHOT/ALLSTAR output for G213. Same as Fig. 3.

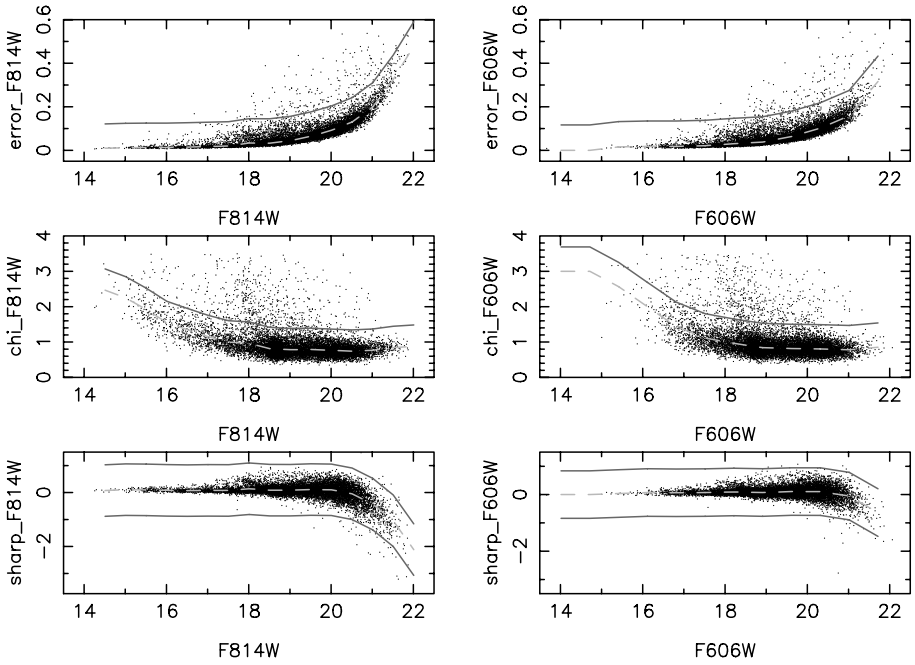

Fig. 5. DAOPHOT/ALLSTAR output for G280. Same as Fig. 3.